Heliyon 8 (2022) e12348

Contents lists available at ScienceDirect

Heliyon

journal homepage: www.cell.com/heliyon

Research article

Compatibility optimization of a polyhedral-shape thermoelectric generator for automobile exhaust recovery considering backpressure effects

Rui Quan [a,b,*], Junhui Wang [a,b], Tao Li [a,b]

[a] Hubei Engineering Research Center for Safety Monitoring of New Energy and Power Grid Equipment, Hubei University of Technology, Wuhan 430068, China
[b] Hubei Key Laboratory for High-efficiency Utilization of Solar Energy and Operation Control of Energy Storage System, Hubei University of Technology, Wuhan 430068, China

ARTICLE INFO

Keywords:
Heat exchanger
Thermoelectric generator
Fin parameters
Compatibility
Multi-objective grey wolf optimizer

ABSTRACT

The output performance of thermoelectric generator using thermoelectric modules can be improved by optimizing the heat exchanger structure, but this may cause compatibility issues in the exhaust heat recovery process, such as high backpressure and poor performance for the internal combustion engine. In this study, a polyhedral-shape heat exchanger-based thermoelectric generator system for vehicle exhaust recovery was constructed for the uniform temperature and easy thermoelectric module layout, and the influencing factors of heat transfer and backpressure was evaluated using a realizable k-ϵ turbulence model, and the influence order was analyzed based on the analysis of variance method. Finally, a multi-objective grey wolf optimizer was used to improve the thermoelectric generator system based on the proposed compatibility performance index and optimization objective function. The findings show that the heat transfer performance and backpressure of heat exchanger is obviously affected by different fin length, fin width, fin intersection angle and fin spacing distance. Compared with the empty cavity structure based one and those without optimization, the optimized fin parameters not only obtain high power and satisfactory thermoelectric conversion efficiency, but also ensure low pressure drop and ideal temperature uniformity, which well meets the compatibility requirements for automobile exhaust recovery application.

1. Introduction

Thermoelectric generators (TEGs) have been a promising green energy technology and became a research hotspot all over the world for they can convert the waste heat into energy [1]. Due to the advantage of having no moving parts and low vibration, thermoelectric modules (TEMs) of high reliability and durability have been widely applied in engines [2], solar energy [3], astronautic tools [4], wireless devices [5], military powertrain [6], industry electronics [7], medical system [8] and wearables [9]. It is well known that the classical internal combustion engines (ICE) can only convert around 25% of their chemical energy into mechanical energy, with the other 75% being used up by exhaust heat, ICE coolant, mechanical friction, and other power losses [10]. To fully harvest the waste heat from exhaust gas, many studied have displayed the development of different automobile exhaust thermoelectric generators (AETEGs). For example, Zhang et al. [11] developed an AETEG system with coolant, the experimental results indicated that it obtained a maximum power of 1002.6 W and a 2.1% thermoelectric conversion efficiency when the flow mass is 480 g/s. Brito et al. [12] proposed a novel AETEG with many conductance heat pipes to protect TEMs from thermal damage. Kim et al [13] brought out an AETEG whose measured maximum power was 350 W when the evaporator surface temperature of heat pipes was 443 K.

Despite of developing advanced thermoelectric materials such as Skutterudite, Half-Heusler and Silicon Germanium [14], structure optimization of heat exchangers and TEMs can increase the output power and system efficiency of TEG. According to the structure and shape of heat exchangers utilized in TEGs, there are cylindrical-shape (CS) [15], polyhedral-shape (PS) [16] and flat plate-shape (FPS) [17] ones. Regardless of the uniform surface temperature distribution, first two ones can be covered with more TEMs than the last one for they are usually manufactured with several symmetrical surfaces. However, the first two have lower average surface temperature and output power than the last one under the same condition [18], and their installation and clamping for TEMs is inconvenient. In all, lots of scholars have focused on AETEG research using the above heat exchangers from the aspect of theoretical

* Corresponding author.
E-mail address: quan_rui@126.com (R. Quan).

https://doi.org/10.1016/j.heliyon.2022.e12348
Received 24 September 2022; Received in revised form 8 November 2022; Accepted 7 December 2022

modelling, numerical simulation and experimental test, which mainly involved the hot and cold side temperatures of TEMs, power generation and system efficiency of AETEG based on different TEMs configurations and heat exchanger dimensions [19, 20].

However, the fin parameters and flow field structure of heat exchanger will change the backpressure (i.e. pressure drop, denoted P_d) of ICE when its exhaust pipe is connected to the inlet of heat exchanger, which leads to terrible power loss. Yang et al. [21] developed an AETEG rated at 300 W, the road test result under Environmental Protection Agency (EPA) highway demonstrated that the maximum backpressure approached 5.58 kPa, and it was increased to 1.54 kPa under urban road conditions. Michos et al. [22] proposed a heat recovery vapor generator using FPS heat exchanger, which caused high backpressure for the exhaust gas and organic fluid. Li et al. [23] proposed a heat exchanger inserted with different optimized dimples, which could balance the pressure drop of heat exchaner, temperature distribution of TEMs and output power of AETEG.

The above literatures review shows that many researchers have focused on the performance investigation and enhancement of heat exchanger or TEG system, some of them optimized the heat exchanger by inserting different fins or designing different inner topologies without considering the caused unwanted backpressure and deteriorative temperature uniformity. As a matter of fact, the influence of small backpressure on the ICE performance is negligible when TEG system is applied in automobile exhaust recovery. However, the increased backpressure will reduce the dynamic performance and increase the emission of ICE to some extent. When the generated maximum power of AETEG is much smaller than the ICE's loss, the AETEG's gain becomes the ICE's loss [24]. Therefore, the performance deterioration and power loss caused by the backpressure (i.e. incompatibility characteristic) should be seriously considered to optimize the structure parameters of heat exchangers.

Considering the PS heat exchanger displays uniform temperature distribution and low backpressure, it is adopted in the TEG development which can be applied in automobile exhaust recovery. Besides, the comprehensive numerical model of TEG system was established to evaluate its influencing factors whose importance degree was investigated based on analysis of variance (ANOVA) method. Then, a compatibility agent model was established for TEG, and validated based on the orthogonal experimental design method and Gauss process regression algorithm according to the proposed compatibility performance index which make a balance among backpressure, output power and temperature uniformity. Finally, the research results based on the optimized fin parameters were compared with other cases to validate the enhanced compatibility performance of TEG system, which provides a theoretical guide for the behavior evaluation and structure optimization of AETEGs without obviously deteriorating the original performance of ICE on the condition of low backpressure for heat exchanger.

2. A PS heat exchanger based TEG

The designed TEG system is shown in Figure 1, and the PS heat exchanger has six heat transfer surfaces which are covered with 30 single TEMs. From inlet to outlet direction of PS heat exchanger, 5 single TEMs above each surface share a common coolant box, and they are labeled as column 1 to 5 in sequence. To obtain uniform cold side temperature of TEMs, all the coolant boxes made of aluminum alloys are connected in parallel, and they are clamped above TEMs with tightening parts. To absorb the exhaust heat as much as possible, brass is utilized to manufacture the proposed PS heat exchanger which is inserted with lots of fins. Due to the small power and low output voltage of a single TEM with low temperature difference between its hot side and cold side, all the TEMs connected in series supply power to external electronic load or charge batteries using a DC/DC converter. To reduce the heat loss, all the uncovered area among heat exchanger, coolant boxes and TEMs is filled with high temperature resistant insulation material made from Zirconia.

3. Effect of inserted fins on the performance of PS heat exchanger

3.1. Geometry and meshing

As shown in Figure 2, the PS heat exchanger is taken for an example to assess the effect of parallel arranged fins on its performance. Where, the symbols of L, W, A and S represent the fin length, fin width, fin

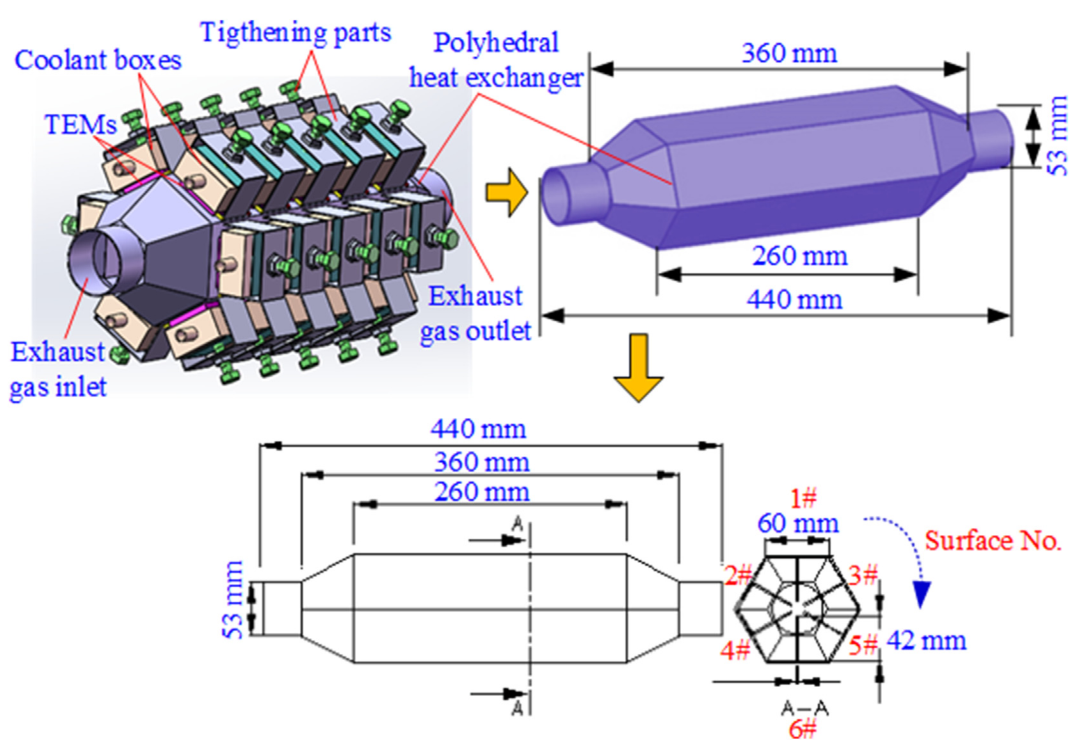

Figure 1. Schematic of the PS heat exchanger based TEG system.

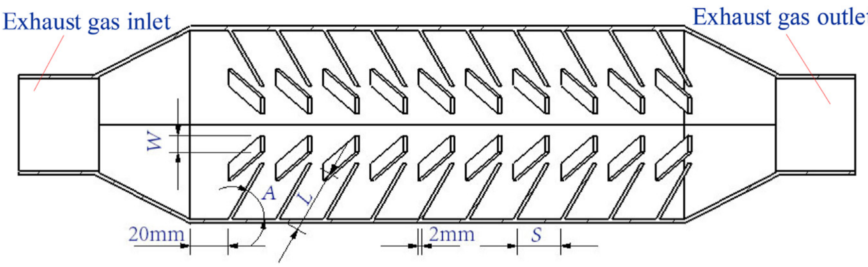

Figure 2. Fin parameters of PS heat exchanger.

intersection angle and fin spacing distance, respectively. To ensure simplified model calculation and make obvious difference between its fluid domains and solid domains, the region out of its internal cavity is full of fluid. Besides, the mesh size is set at 2 mm, and each mesh has an average mass greater than 0.84. Finally, to ensure fast convergence, coarse mesh is set as 20 million (the corresponding parameters of wall-normal is $\mu_f \Delta y / k_\nu < 2$), fine mesh is set to be 25 million (the corresponding parameters of wall-normal is $\mu_f \Delta y / k_\nu < 1$), and finer mesh is fixed at 30 million (the corresponding parameters of wall-normal is $\mu_f \Delta y / k_\nu < 0.2$), where μ_f represents the friction velocity, k_ν means the kinematic viscosity, and Δy is the wall-normal distance.

3.2. Numerical model of heat exchanger

To ensure simplified calculation for the established model, the following assumptions are proposed:

(1) Exhaust gas is incompressible and has steady flow rate.
(2) The inlet exhaust of PS heat exchanger is evenly distributed.
(3) The heat radiation of PS heat exchanger and heat loss among TEMs are ignored.
(4) Considering the complex composition of exhaust gas, the air is used instead of it as the fluid material.

At present, the main turbulence models used in CFD software include Spalart-Allmaras model, k-ϵ model, k-ω model and Reynolds stress model, and the k-ϵ model is practice for engineering calculation because of its high accuracy.

The k-ϵ models package includes the standard k-ϵ model, RNG k-ϵ model and realizable k-ϵ model. The last two kinds of models are improved and developed based on the standard one. The last one has improved the turbulence viscosity formula and added a new dissipation rate transfer equation based on the original turbulent dynamic and the turbulent dissipation rate equations, it has more accurate solutions in strong streamline bending, vortex and rotation situations, and has better analysis and prediction performance of complex secondary flow and flow separation problems than other k-ϵ models. Considering the hot exhaust is turbulent and it has more secondary flows inside the PS heat exchanger, the heat transfer and flow field calculation based on a realizable k-ϵ turbulence model are described by Eqs. (1) and (2), respectively.

$$\frac{\partial(u_i k)}{\partial x_i} = \frac{\partial}{\partial x_i}\left[\left(\mu + \frac{\mu_t}{\delta_\epsilon}\right)\frac{\partial k}{\partial x_i}\right] + P_k - \varepsilon \tag{1}$$

$$\frac{\partial(u_i \varepsilon)}{\partial x_i} = \frac{\partial}{\partial x_i}\left[\left(\mu + \frac{\mu_t}{\delta_\varepsilon}\right)\frac{\partial \varepsilon}{\partial x_i}\right] + C_1 S\varepsilon - C_2\frac{\varepsilon^2}{k + \sqrt{\nu\varepsilon}} \tag{2}$$

where $\mu_t = \frac{k^2}{\varepsilon A_0 + A_S u^* k}$, $C_1 = \max\left[\frac{kS}{kS+5\varepsilon}, 0.43\right]$, $u^* \equiv \sqrt{S_{ij}^2 + \Omega_{ij}^2}$, $\Omega_{ij} = \frac{1}{2}\left(\frac{\partial u_i}{\partial x_j} - \frac{\partial u_j}{\partial x_i}\right)$, $A_S = \sqrt{6}\cos\varphi$, $\varphi = \frac{1}{3}\cos^{-1}\left(\sqrt{6}\ \frac{S_{ik}S_{ki}}{S_{ij}^2}\right)$, $S_{ij} = \frac{1}{2}\left(\frac{\partial u_i}{\partial x_j} + \frac{\partial u_j}{\partial x_i}\right)$, $\delta_k = 1.0$, $\delta_\varepsilon = 1.2$, $C_2 = 1.9$, $A_0 = 4.0$. P_k, k, μ_t, ϵ and S are the shear production, turbulence kinetic energy, kinetic viscosity, turbulent energy dissipation rate and mean modulus of strain rate tensor, respectively. u_1, u_2 and u_3 represent the x-axis, y-axis and z-axis velocity components of fluid flow, respectively. x_1, x_2 and x_3 correspond to the x, y and z directions, respectively. Finally, the above model is established based on ANSYS FLUENT software to simulate the TEG system performance.

Although the exhaust around the middle area of the PS heat exchanger is completely turbulent, the one near the wall of the heat exchanger is laminar, and the gradient of velocity and temperature varies greatly. The accurate calculation of gradients is very important for the simulation calculation of heat transfer, it needs more dense grids to capture these gradients, consumes longer time and more computing resources, and leads to poor convergence because of the dense grids. In this regard, the semi-empirical formula of wall function is adopted in Fluent simulation software to solve the above heat transfer problems, which ensures the physical variables on the wall are related to the ones in the center of the completely turbulent region, and greatly simplifies the calculation process without modifying the turbulence model.

The commonly used Wall functions include the Standard, Scalable, Non-equilibrium and Enhanced Wall functions, among which the Scalable ones improve the calculation accuracy of the standard one especially when the Wall distance is less than 11. Therefore, Scalable Wall functions are selected for the heat exchanger simulation in this section.

To calculate the heat transfer and flow field with ANSYS FLUENT software, boundary conditions of numerical simulation are listed in Table 1. Air is selected as the fluid materials, the classical heat transfer coefficient is fixed at 20 W/(mK), and the inlet and outlet diameter of coolant box is set to be 16 mm. Besides, the relative outlet pressure of PS heat exchanger is set as 0 Pa for ambient air is connected to it, and the calculation of both turbulent dissipation energy rate and kinetic energy is carried out with the second order upwind. To alleviate the calculation complexity and reduce the divergence of iterative process, the minimum convergence tolerance of governing equations is set to be 10^{-6}.

Table 1. Boundary conditions of numerical simulation.

Parameter	Value
Inlet flow velocity	20~40 m/s
Inlet flow temperature	323 °C
Ambient temperature	23 °C
Coolant flow rate	5000 L/h
Thermal conductivity of *P*-type thermoelectric legs	2.0 W/(mK)
Thermal conductivity of *N*-type thermoelectric legs	2.5 W/(mK)
Seebeck coefficient of *P*-type thermoelectric legs	215 (μV/K)
Seebeck coefficient of *N*-type thermoelectric legs	-215 (μV/K)
Electrical resistivity of PN thermoelectric legs	1.04×10^{-5} (Ωm)
TEM size	40 mm × 40 mm × 4 mm
Coolant box size	300 mm × 60 mm × 21 mm
Coolant box thickness	1 mm
Radiator power	100 W
Water pump power	40 W

3.3. Equivalent circuit model of TEG

The thermal resistance of thermoelectric legs (denoted R_{PN}) is expressed by Eq. (3).

$$R_{PN} = \frac{\delta_{PN}}{A_{PN}\lambda_{PN}} \tag{3}$$

where A_{PN}, δ_{PN} and λ_{PN} are referred to the effective area, thickness and thermal conductivity of PN thermoelectric legs.

For a single TEM, according to its PN thermoelectric legs number N_{PN}, its internal resistance (denoted R_{In}) can be calculated using Eq. (4) according to leg length (denoted l_P and l_N, respectively), electricity resistivity (denoted μ_P and μ_N, respectively) and effective area (denoted A_P and A_N, respectively) of PN thermoelectric legs [25].

$$R_{In} = N_{PN}l_P\mu_P/A_P + N_{PN}l_N\mu_N/A_N \tag{4}$$

According to the TEM datasheet of TEHP1-1264-0.8, the leg length of PN thermoelectric legs is equal to 1.4 mm, N is 128. Besides, the effective heat transfer area of TEM is 1600 mm^2, the height of PN thermoelectric legs is 2.2 mm, and the height of ceramic plate is 0.8 mm. In this regard, R_{In} is calculated to be about 1.59 Ω.

According to the hot side (denoted T_H) and cold side temperature (denoted T_L) of a TEM, its open-circuit voltage (denoted V_{oc}) and practical output voltage (denoted V_L) can be calculated using the following formulas (Eqs. (5) and (6)) [25].

$$V_{oc} = N(\alpha_p - \alpha_n)(T_H - T_L) = N\alpha_{PN}\Delta T \tag{5}$$

$$V_L = V_{oc} - I_L R_{In} \tag{6}$$

where α_{PN} represents the relative Seebeck coefficient of PN couples, α_p means the Seebeck coefficient of P-type thermoelectric legs, and α_n refers to the one of N-type thermoelectric legs, I_L is the output current.

For the output characteristic of a single TEM is similar to the TEG system without considering the dynamic process, the internal resistance R_{TEG} and open-circuit voltage U_{oc} of the TEG system are expressed by Eqs. (7) and (8), respectively.

$$R_{TEG} = \sum_{i=1}^{30} R_{In}(i) \tag{7}$$

$$U_{oc} = \sum_{i=1}^{30} V_{oc}(i) \tag{8}$$

For the TEG system, its practical voltage (denoted U) and real power (denoted P_{all}) can be defined using Eqs. (9) and (10).

$$U = U_{oc} - I_L R_{TEG} = \frac{\sum_{i=1}^{30} V_{oc}(i)R_L}{\sum_{i=1}^{30} R_{In}(i) + R_L} \tag{9}$$

$$P_{all} = \frac{U_{oc}^2 R_L}{(R_{TEG} + R_L)^2} = \frac{\left(\sum_{i=1}^{30} V_{oc}(i)\right)^2 R_L}{\left(\sum_{i=1}^{30} R_{In}(i) + R_L\right)^2} \tag{10}$$

When the load resistance R_L is equal to R_{TEG}, P_{all} reaches a maximum value (denoted P_{max}) which is described by Eq. (11).

$$P_{max} = \frac{U_{oc}^2}{4R_{TEG}} = \frac{\left(\sum_{i=1}^{30} V_{oc}(i)\right)^2}{4\sum_{i=1}^{30} R_{In}(i)} \tag{11}$$

3.4. Validation of numerical model

As shown in Figure 3, a TEG experimental platform is set up to validate the proposed numerical model. Considering the PS heat exchanger without fins has almost the same modelling process as the one with fins,

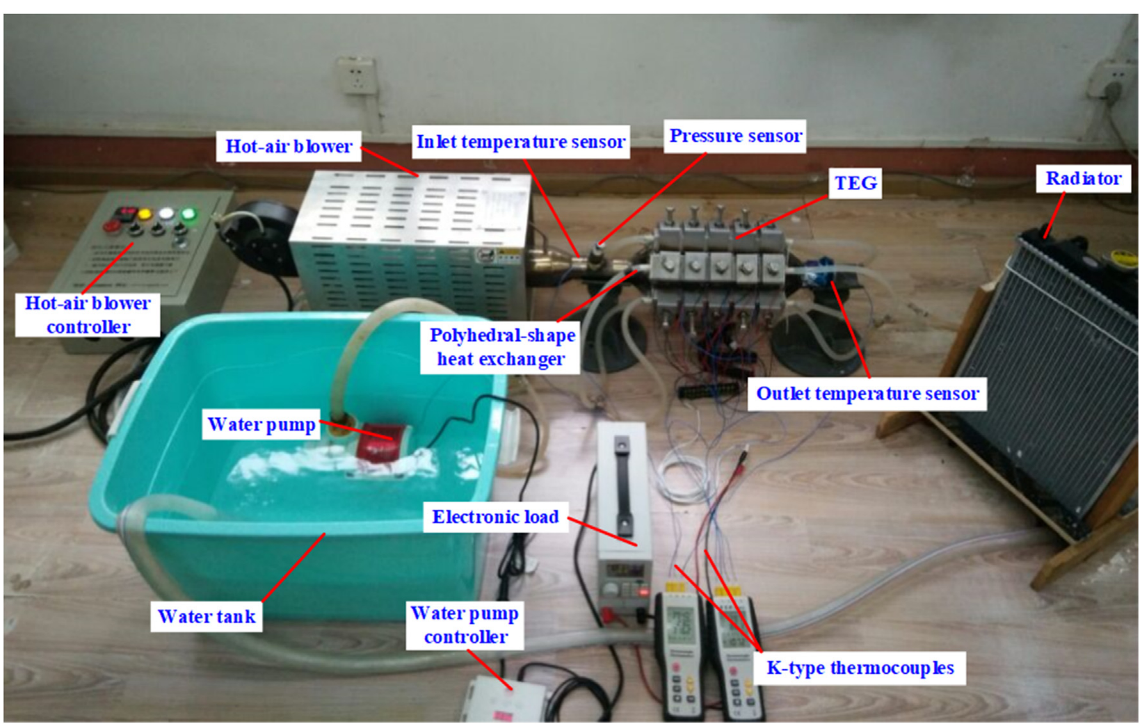

Figure 3. TEG experimental platform.

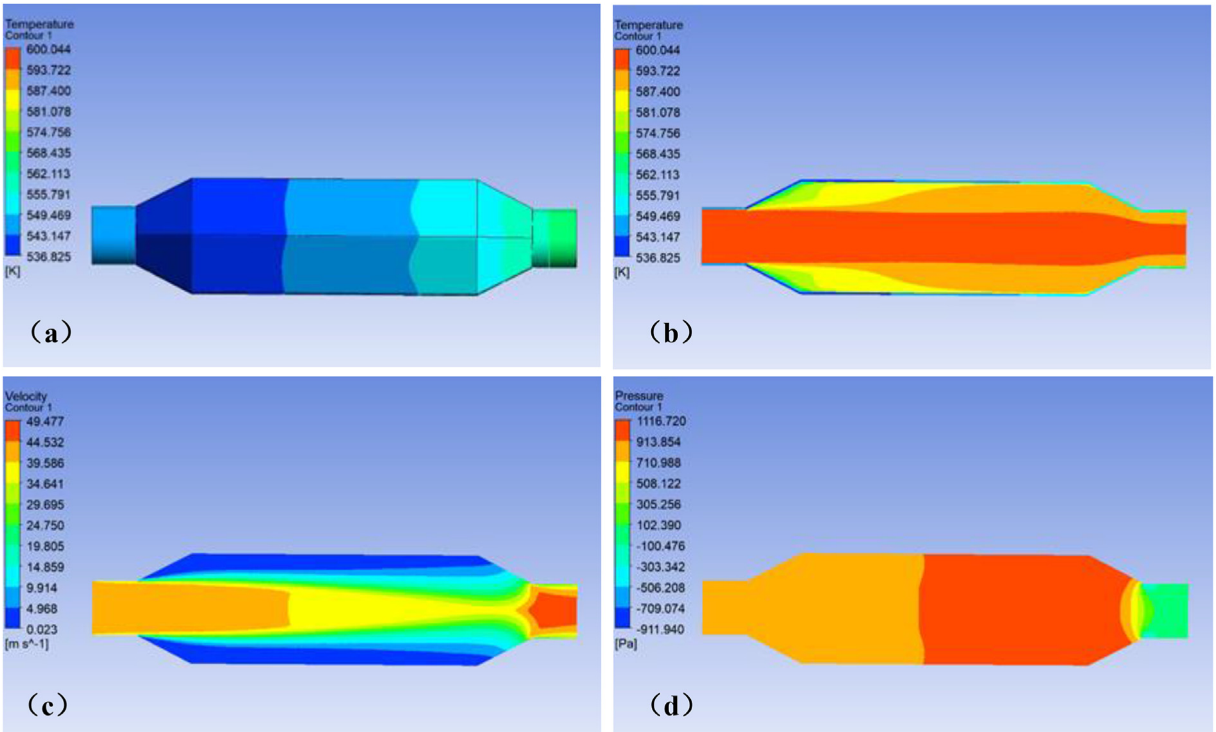

Figure 4. Temperature map of the empty cavity structure based PS heat exchanger. (a) surface temperature; (b) internal temperature; (c) fluid velocity; (d) fluid pressure.

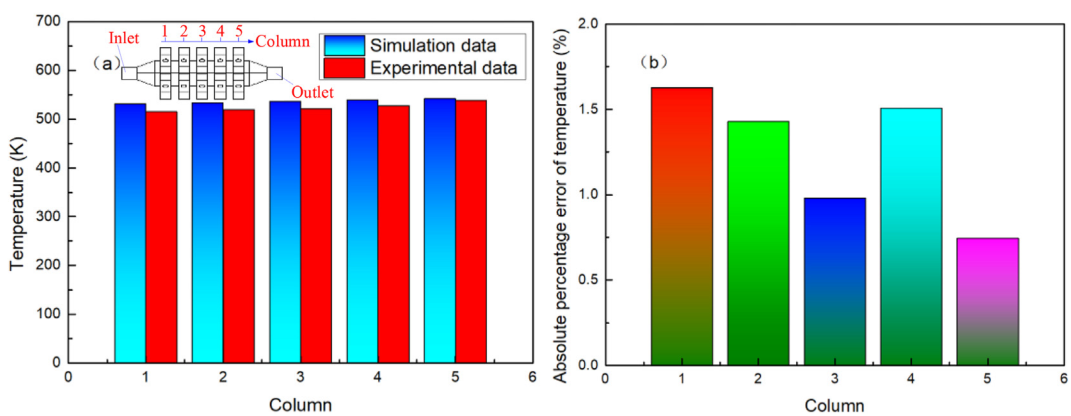

Figure 5. Simulation and experimental comparison of temperature distribution. (a) surface temperature; (b) absolute percentage error.

and the former has lowest pressure drop, the above numerical model validation work is conducted on the PS heat exchanger with empty cavity structure. To simulate the ICE operation with different inlet temperatures and flow rates, the hot-air blower provides exhaust heat to the PS heat exchanger with different rotating speeds. Considering the six symmetrical surfaces of PS heat exchanger have similar temperature distribution, each surface temperature is measured with six K-type thermocouples which are installed at the center points of the hot side temperature locations corresponding to all the TEMs.

The temperature map of empty cavity structure based PS heat exchanger without any TEMs nor cooling boxes is shown in Figure 4, and the comparative external surface temperature distribution between experimental data and simulation result is displayed in Figure 5. Obviously, the exhaust flows quickly through the internal area of PS heat exchanger because of the wide empty cavity, then it increases from inlet to outlet direction. Besides, as shown in both Figures 4(a) and 5(a), the inlet area of heat exchanger has lowest surface temperature, and its outlet area has higher surface temperature because of the caused gas eddy. Figure 5(b) indicates that the experimental tests tie well with the simulation results, for the absolute percentage error is below 1.65%.

When the 30 TEMs and 6 cooling boxes are installed according to the schematic shown in Figure 1, the output performance comparison of TEG system between experimental measurement and numerical data with different inlet flow of exhausts (i.e. 20 m/s, 30 m/s, 35 m/s and 40 m/s, respectively) is shown in Figure 6. Obviously, when the open-circuit voltage is 44.08 V (see Figure 6a), the maximum absolute error of between simulation data and experimental data is 1.09 V; when the output power is 10.69 W (see Figure 6b), its maximum absolute error 0.41 W. Considering the maximum absolute percentage error shown in Figure 6c and 6d is below 3.9%, it can be concluded that the established numerical model is suitable for the heat transfer evaluation and the power prediction of TEG system.

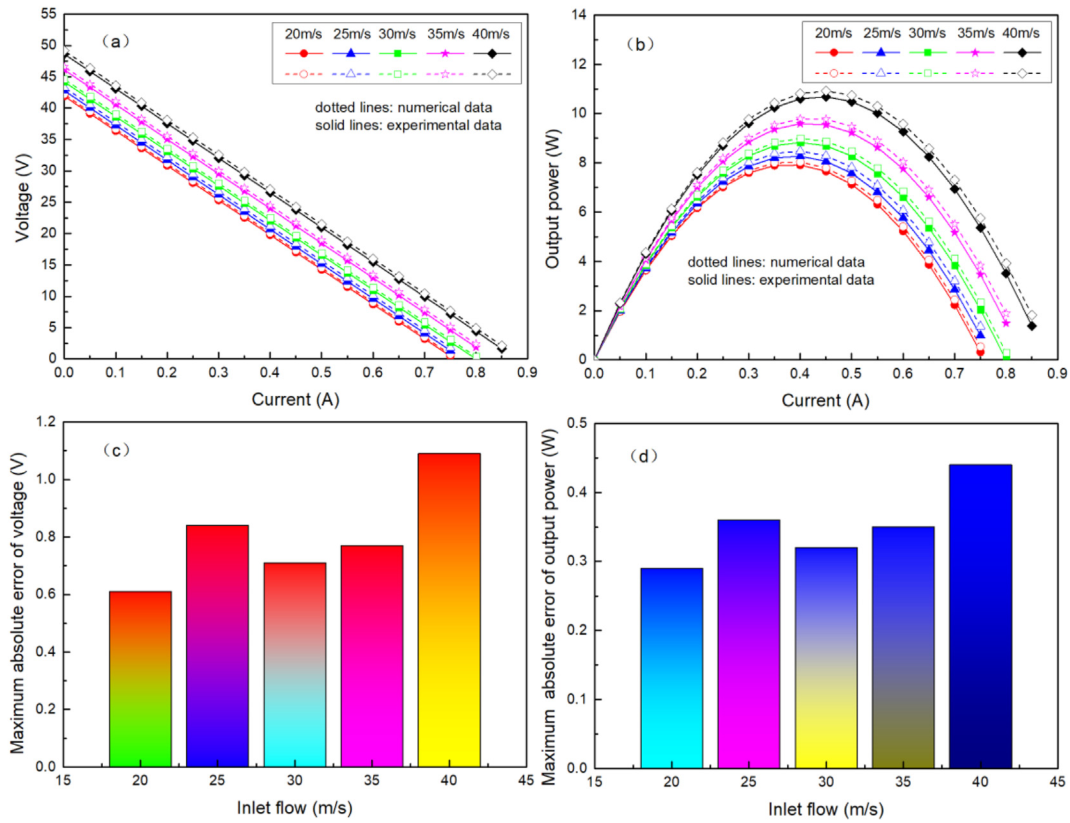

Figure 6. Output performance comparison of TEG system between experimental data and numerical data. (a) voltage; (b) power. (c) maximum absolute error of open-circuit voltage; (d) maximum absolute error of power.

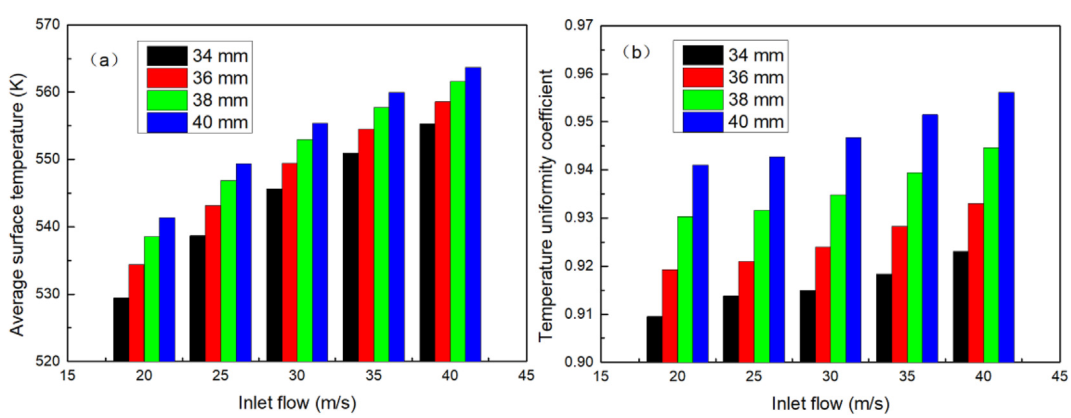

Figure 7. Effect of L on the temperature distribution. (a) T_{ave}; (b) γ.

3.5. Effect of fin parameters on the heat transfer performance

Improved temperature uniformity of heat exchanger helps to minimize the buckets effect caused by the TEMs of lowest temperature difference, and avoid current-circulation loss of TEMs connected in parallel [26]. Thus, to verify the effect of fin parameters on the heat transfer performance of the PS heat exchanger, the temperature uniformity coefficient γ corresponding to the 30 detected locations temperatures can be calculated by Eq. (12).

$$\gamma = 1 - \frac{1}{30}\sum_{i=1}^{30}\frac{\sqrt{(T_i - T_{ave})^2}}{T_{ave}} \tag{12}$$

where T_i ($i = 1,2, \ldots, 30$) are the detected surface temperatures corresponding to the hot sides of 30 TEMs, and T_{ave} is the average surface temperature of heat exchanger.

The effect of fin length on the average surface temperature and temperature uniformity coefficient of PS heat exchanger with different inlet flow rates is shown in Figure 7 ($W = 8$ mm, $A = 80°$, $S = 30$ mm). Obviously, increasing fin length and inlet flow rate contribute to the enhanced average surface temperature (see Figure 7a) and temperature uniformity (see Figure 7b) on the same occasion, and increases the TEG's maximum power to some extent. T_{ave} is increased by 8.4 °C at a maximum inlet flow rate of 40 m/s as L ranges from 34 mm to 40 mm, which can be explained by the enhanced convective heat transfer caused by increased inlet flow rate and heat transfer area. In addition, the

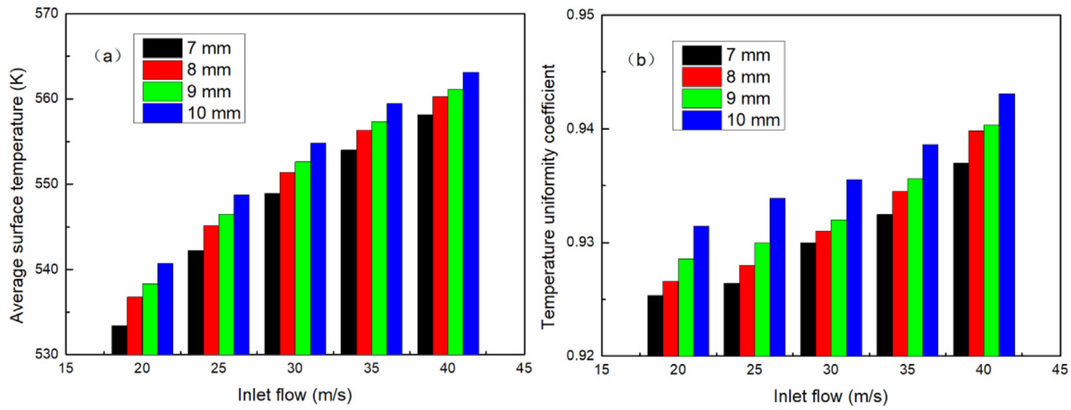

Figure 8. Effect of W on the temperature distribution. (a) T_{ave}; (b) γ.

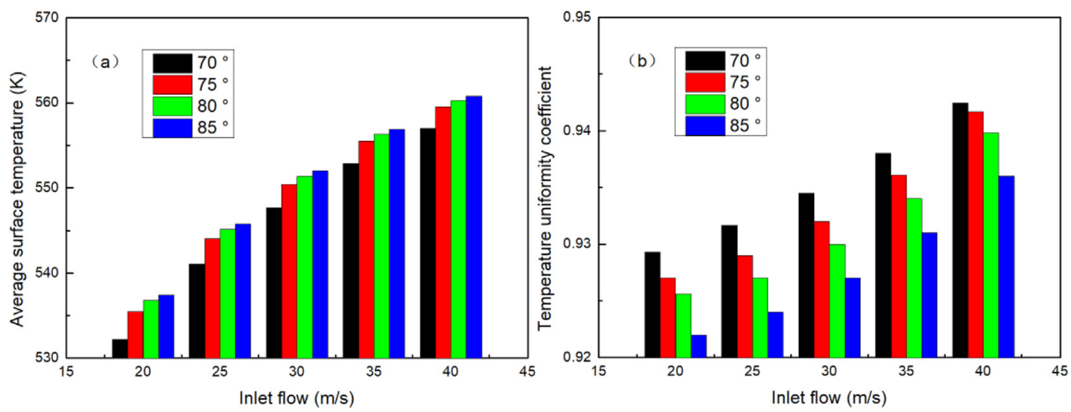

Figure 9. Effect of A on the temperature distribution. (a) T_{ave}; (b) γ.

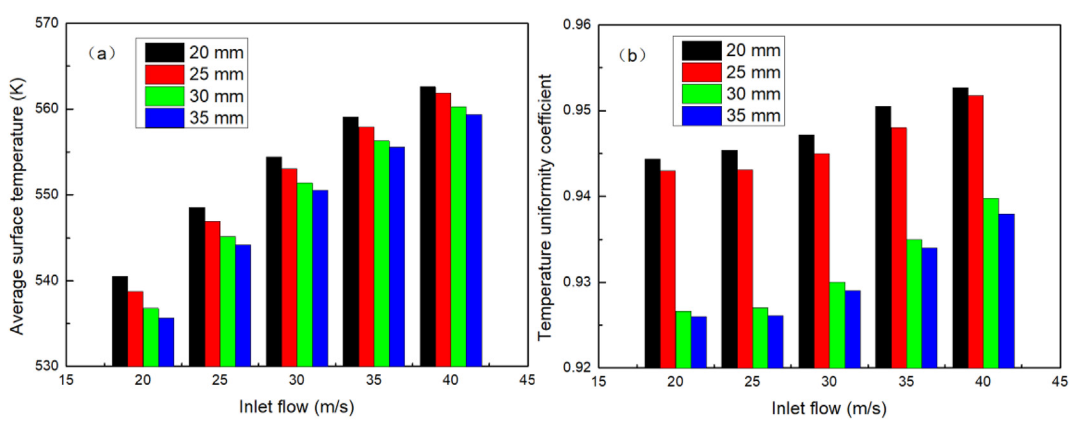

Figure 10. Effect of S on the temperature distribution. (a) T_{ave}; (b) γ.

maximum difference of γ is only 0.04 (see Figure 7b), and γ is increased by 0.033 when inlet flow rate is 40 m/s and the maximum L is 40 mm.

Figure 8 shows the effect of fin width with different inlet flow rates (L = 37 mm, A = 80°, S = 30 mm). It can be observed that the increased T_{ave} is 5.1 °C (see Figure 8a) and the maximum difference of γ is only 0.006 (see Figure 8b). Therefore, increasing fin width has little effect on improving the temperature distribution of heat exchanger.

Figure 9 shows the effect of fin intersection angle with different inlet flow rates. Similarly, increasing fin intersection angle can improve the thermal characteristic of PS heat exchanger. When A is 85° and the inlet flow rate is 40 m/s, T_{ave} is increased by 3.79 °C (see Figure 9a). Specifically, there is almost no obvious average surface temperature improvement when A is less than 75°, and the increment is nearly saturated when A is larger than 80°.

However, γ is inversely proportional to fin intersection angle, the maximum difference of γ is below 0.007 at the largest inlet flow rate of 40 m/s (see Figure 9b).

Figure 10 shows effect of fin spacing distance with different inlet flow rates. As shown in Figure 10a and 10b, both T_{ave} and γ are inversely proportional to fin spacing distance with the same inlet flow for the effective heat transfer area can be enlarged with decreasing S.

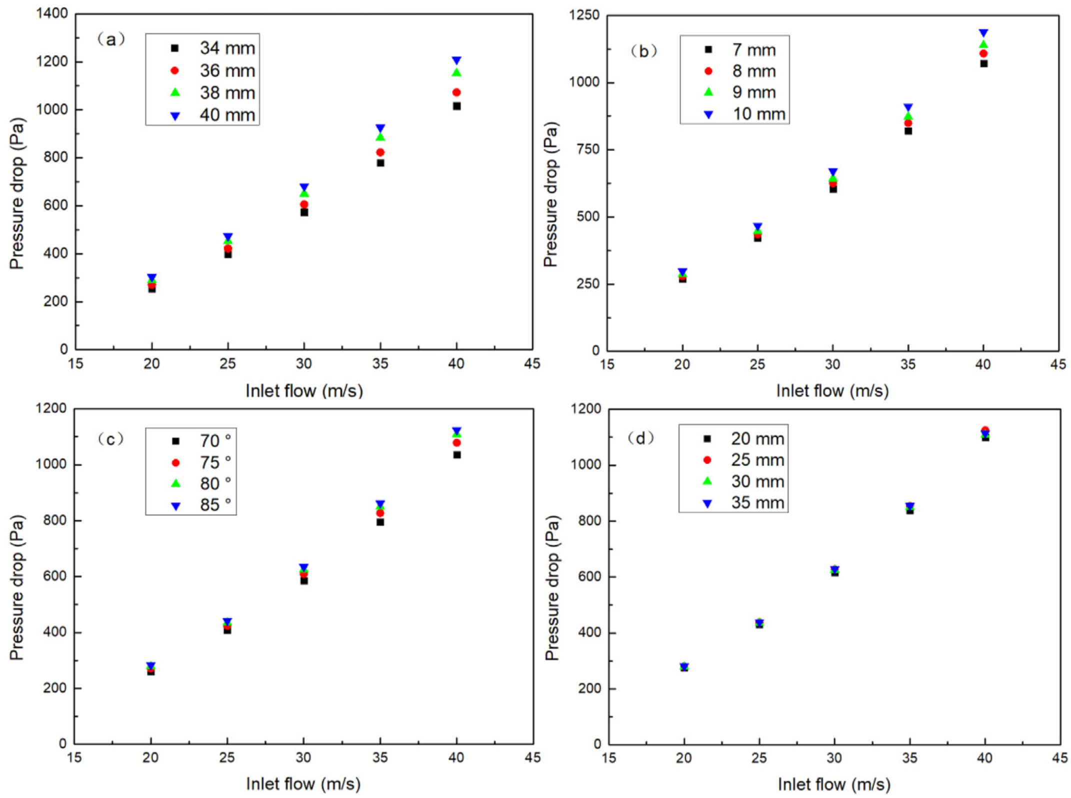

Figure 11. Effect of fins parameters on the pressure drop. (a) L; (b) W; (c) A; (d) S.

3.6. Effect of fin parameters on the pressure drop

Based on the boundary conditions listed in Table 1, Figure 11 shows the effect of different L, W, A and S on the pressure drop (see Figure 11a–d, respectively). Obviously, both pressure drop and pressure drop deviation are proportional to inlet flow rate, and the former is increased from 48.4 Pa to 193.8 Pa as L changes from 34 mm to 40 mm and inlet flow increases from 20 m/s to 40 m/s (see Figure 11a). Figure 11b demonstrates that increasing fin width leads to increased pressure drop which approaches 1188. 3 Pa when the maximum inlet flow rate is 40 m/s ($W = 10$ mm). As shown in Figure 11c, the pressure drop is increased by 88.9 Pa when the maximum inlet flow rate is 40 m/s ($A = 85°$). Figure 11d shows that the pressure drop is increased by 25.3 Pa at maximum inlet flow rate of 40 m/s, it can be concluded that the effect of S on the ICE emissions is negligible to some extent.

3.7. Analysis of variance for the effect of fin parameters

Orthogonal experimental design is an effective method to research on multi-factor and multi-level systems, it selects some strong representativeness from the whole experiment with orthogonality, which ensures the experimental results conform to the actual situation by reducing the workload [27, 28]. Considering the compatibility optimization precision, the proposed factor level of fin parameters is listed in Table 2. The fin parameters are divided into four levels which generates 16 experimental samples, and the possible interaction effects between the variables is ignored.

To evaluate the influence order of fin parameters on the performance of the PS heat exchanger, the analysis of variance (ANOVA) method is adopted for it can effectively distinguish the variation of the experimental results caused by the design variables from that caused by the experimental errors [29], and it is suitable for the significance analysis of the above fin parameters on the compatibility performance of TEG system. Firstly, the sum of squared experimental variable deviations, squared experimental error deviations and squared total deviations (denoted S_T) are calculated. Secondly, the degree of freedom is computed. Finally, the sum of mean squared deviations of experimental variables and the sum of mean squared experimental error deviations are calculated.

Table 2. Factor level of fin parameters.

Level	Fin parameters			
	L	W	A	S
1	34 mm	7 mm	70°	20 mm
2	36 mm	8 mm	75°	25 mm
3	38 mm	9 mm	80°	30 mm
4	40 mm	10 mm	85°	35 mm

For S_T, it reflects the experimental results difference caused by all the data errors and can be expressed using Eqs. (13) and (14), respectively [30, 31].

$$S_T = \sum_{k=1}^{n} (x_k - \overline{x})^2 \tag{13}$$

$$\overline{x} = \frac{1}{n} \sum_{k=1}^{n} x_k \tag{14}$$

where n is the total number of experiments, x_k represents the kth experimental result.

ANOVA divides all the data error into intra-group and inter-group one. The former reflects the experimental results difference caused by the level variation of the experimental variable, which can be expressed as the sum of squared deviations of the experimental variable (denoted as S_k). The latter means the experimental results difference caused by the experimental error existing within the level or the inherent difference of the data, and it can be expressed by the sum of squared experimental error deviation (denoted as S_e). S_k and S_e can be calculated by Eqs. (15), (16), and (17), respectively.

$$S_k = \sum_{i=1}^{m} l_i(\overline{x_i} - \overline{x})^2 \tag{15}$$

$$\overline{x_i} = \frac{1}{l_i}\sum_{j=1}^{l_i} x_{ij} \tag{16}$$

$$S_e = S_T - \sum_{z=1}^{g} S_z \tag{17}$$

where m is the level number of experimental variable k (i.e. L, W, A and S), l_i is the total experiment number at the ith level of experimental variable k, x_{ij} is the jth experimental result of the experimental variable k at the ith level, g is the total number of experiment variables, S_z is the sum of squared deviations of the zth experimental variable.

For the total degree of freedom (DOF) ν_T, the DOF of experiment variable k (denoted ν_k) and experiment error (denoted ν_e) can be calculated by Eqs. (18), (19), and (20), respectively.

$$\nu_T = n - 1 \tag{18}$$

$$\nu_k = m - 1 \tag{19}$$

$$\nu_e = \nu_T - \sum_{z=1}^{g} \nu_z \tag{20}$$

where ν_Z is the DOF of the zth experimental variable.

The sum of mean squared deviations of the experimental variable (denoted M_k) and mean squared experimental error deviations (M_e) can be called mean square of inter-group and intra-group, respectively. They are equal to the ratio of the sum of the squared deviation to the DOF, which can be calculated by the following formulas (Eqs. (21) and (22)).

$$M_k = \frac{S_k}{\nu_k} \tag{21}$$

$$M_e = \frac{S_e}{\nu_e} \tag{22}$$

If M_k is smaller than M_e, the experimental variable k has limited influence on the experimental results, and they can be incorporated into the experimental errors to recalculate the DOF and the sum of mean squared experimental error deviations.

For the joint hypotheses test (i.e. F-test), F value reflects the influence of experimental variables (i.e. fin parameters) on the experimental result. The larger F value is, the more obvious influence on the experimental result will be. F value is described by Eq. (23).

$$F = \frac{M_k}{M_e} \tag{23}$$

Table 3. The influence factor analysis results of average surface temperature.

Name	L	W	A	S	e
S_k	215.2	75.19	25.87	29.98	0.77
ν_k	3	3	3	3	3
M_k	71.73	10067.34	3502.74	335.62	418.87
F value	281.26	98.27	33.82	39.18	–
Critical value $F_{0.01}$	29.50	29.50	29.50	29.50	–
Critical value $F_{0.05}$	9.28	9.28	9.28	9.28	–
Critical value $F_{0.1}$	5.39	5.39	5.39	5.39	–

Table 4. The influence factor analysis results of temperature uniformity.

Name	L	W	A	S	e
S_k	0.001078	0.000048	0.000219	0.000705	0.000134
ν_k	3	3	3	3	6
M_k	0.000359	0.000016	0.000073	0.000235	0.000022
F value	16.07	–	3.27	10.52	–
Critical value $F_{0.01}$	9.78	–	9.78	9.78	–
Critical value $F_{0.05}$	4.76	–	4.76	4.76	–
Critical value $F_{0.1}$	3.29	–	3.29	3.29	–

where F represents the influence significance of the corresponding experimental variable k on the experimental results. In this study, the sensitivity levels are set as 0.01, 0.05, and 0.1, respectively.

According to the above equations, the influence factor analysis results regarding the average surface temperature, temperature uniformity and pressure drop of the polyhedral-shape heat exchanger are listed in Tables 3, 4 and 5, respectively .

As shown in Table 3, the F value of L, W, A and S is greater than the critical value $F_{0.01}$, which indicates that L, W, A and S obviously affect the internal structure and heat transfer performance of the PS heat exchanger, and they are significant influencing factors of the temperature distribution. In all, the influence order on the average surface temperature by comparing the sum of mean squared deviation can be summarized as: $L > W > S > A$.

Table 4 shows that the F value of both L and S is greater than the critical value $F_{0.01}$, the F value of A is between $F_{0.01}$ and $F_{0.05}$, and the temperature distribution inside heat exchanger can be obviously enhanced by them, which demonstrates that L, S and A are also the highly significant influencing factor of the temperature uniformity. Moreover, as W has been incorporated into the experimental error, its influence on the temperature uniformity is negligible, which avoids the F value calculation. Similarly, the influence order on the temperature uniformity is: $L > S > A > W$.

Table 5 shows that the sum of mean squared deviation of L, W and A is larger than the sum of mean squared experimental error deviation. Thus, L, W and A are the primary influencing factors for the pressure drop of heat exchanger, while S is the secondary influencing factor. Furthermore, the F value of both L and W is larger than their $F_{0.01}$, and the F value of A is larger than its $F_{0.05}$. In all, it indicates that increased L, W and A will prevent exhaust gas from passing through the heat exchanger, and they are the highly significant influencing factors for its pressure drop. As S has been incorporated into the experimental error, its influence on the pressure drop and F value is negligible. Thus, the influence order on the pressure drop is: $L > W > A > S$.

4. Compatibility optimization

4.1. Gauss process regression

Gauss process regression establishes a regression model for the nonparametric model probability, and it suitable for the posterior eval-

Table 5. The influence factor analysis results of pressure drop.

Name	L	W	A	S	e
S_k	108220.73	30202.03	10508.21	1006.87	1506.37
ν_k	3	3	3	3	3
M_k	36078.58	10067.34	3502.74	335.62	418.87
F value	86.13	24.03	8.36	–	–
Critical value $F_{0.01}$	9.78	9.78	9.78	–	–
Critical value $F_{0.05}$	4.76	4.76	4.76	–	–
Critical value $F_{0.1}$	3.29	3.29	3.29	–	–

uation and accurate prediction of unknown inputs. The mean absolute percentage error (*MAPE*) describes the deviation between the actual value and the prediction value. The smaller the *MAPE*, the higher the model accuracy. *MAPE* can be described by Eq. (24).

$$MAPE=\frac{100\%}{N_G}\sum_{i=1}^{N_G}\left|\frac{y_i-f_i}{y_i}\right| \tag{24}$$

where N_G is the samples number, y_i represents simulation value of the ith sample, f_i corresponds to the regression model prediction value of the ith sample.

According to the gauss process regression method described in reference [32, 33], the fitting accuracy of gauss process regression agent model of the PS heat exchanger is shown in Figure 12, the x-axis and y-axis respectively correspond to the simulation data and prediction value of the above 16 orthogonal experiment samples, and the diagonal of $y = x$ means their contour line. The three-scatter diagrams corresponding to the fitting accuracy of average surface temperature, temperature uniformity and pressure drop indicate that all the scatter points are close to the blue diagonal lines. Besides, the *MAPE* of T_{ave}, γ and P_d is 0.037%, 0.256% and 0.11%, respectively, which validates that the simulation value is almost equal to the prediction result, and the fitting accuracy of the proxy model is acceptable.

4.2. Compatibility optimization objective function

To enhance the compatibility performance of TEG system for automobile exhaust recovery, the coupling relationship among the performance of PS heat exchanger should be taken into account. In this study, highest T_{ave}, uniform γ and lowest P_d are the optimization objectives for the proposed heat exchange, which are described by Eqs. (25), (26) and (27), respectively. In this regard, the corresponding constraint condition is shown in Eq. (28).

$$\max f_T\ (L,W,A,S) \tag{25}$$

$$\max f_\lambda\ (L,W,A,S) \tag{26}$$

$$\min f_{\Delta P}\ (L,W,A,S) \tag{27}$$

$$\text{s.t. } L\in X1,\ W\in X2,\ A\in X3,\ S\in X4 \tag{28}$$

where f_T, f_λ and $f_{\Delta P}$ are the T_{ave} function, γ function and P_d function of heat exchanger. X1, X2, X3 and X4 are the design spaces of L, W, A and S. The ranges of X1, X2, X3 and X4 are set to be [34 mm, 40 mm], [7 mm, 10 mm], [70°, 85°] and [20 mm, 35 mm], respectively.

4.3. Multi-objective optimization algorithm method

Grey Wolf Optimizer (GWO) is a new swarm intelligence optimization algorithm, which has the advantages of fast convergence, few parameters adjustment and simple implementation. It mainly includes social hierarchy, surrounding prey, searching prey and attacking prey, and it keeps approaching until finding the optimal solution in an iterative way [34].

The Multi-Objective Grey Wolf Optimizer (MOGWO) [35] introduces multi-objective processing mechanisms based on the traditional grey wolf algorithm. The first one introduces an external population archive to store the optimal individuals in each iteration, and updates the internal individuals of the population according to the dominance relationship. If a new individual is dominated by an individual in the archive, it will not be added to the archive. If a new individual dominates one or more individuals in the archive, it will be added to replace the individuals dominated by it. If the new individual and the individual in the archive do not dominate each other, they will not be added to the archive. The second one is to optimize the leading wolf selection mechanism. The archive space includes all the non-dominated optimal solutions generated in the iteration process, and selects the leading wolf by roulette.

According to the proposed compatibility optimization objective function, MOGWO is utilized to optimize the compatibility performance

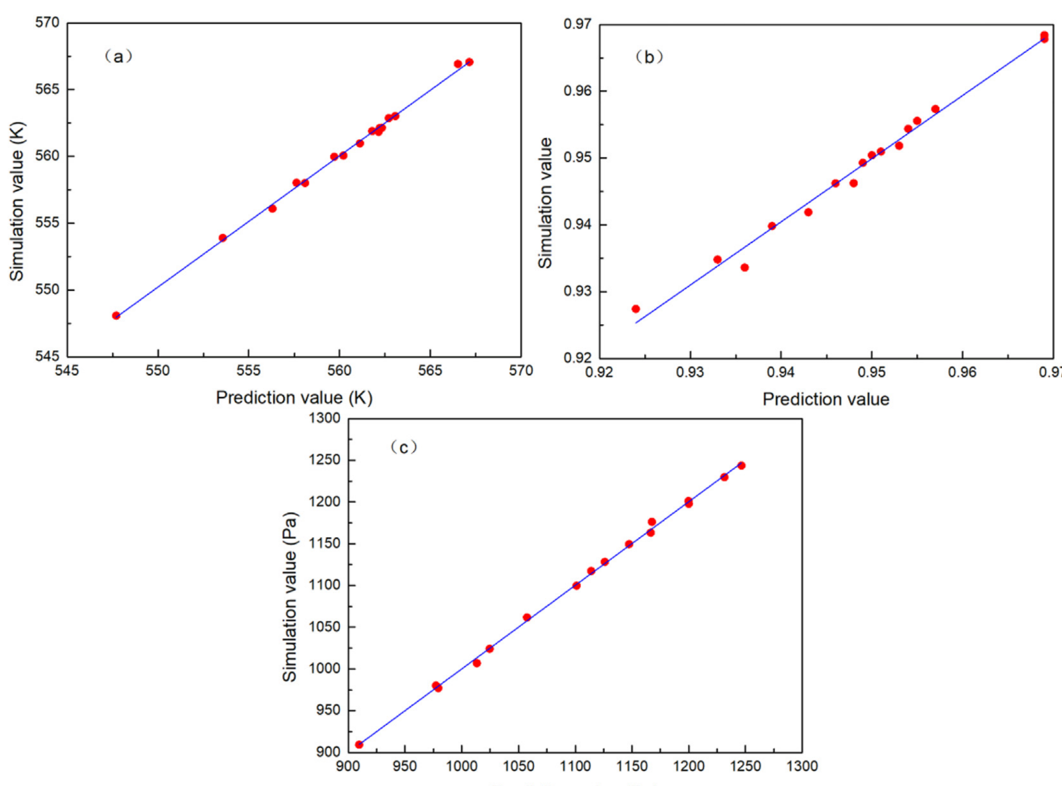

Figure 12. Fitting accuracy scatter diagram of gauss process regression proxy model. (a) T_{ave}; (b) γ; (c) P_d.

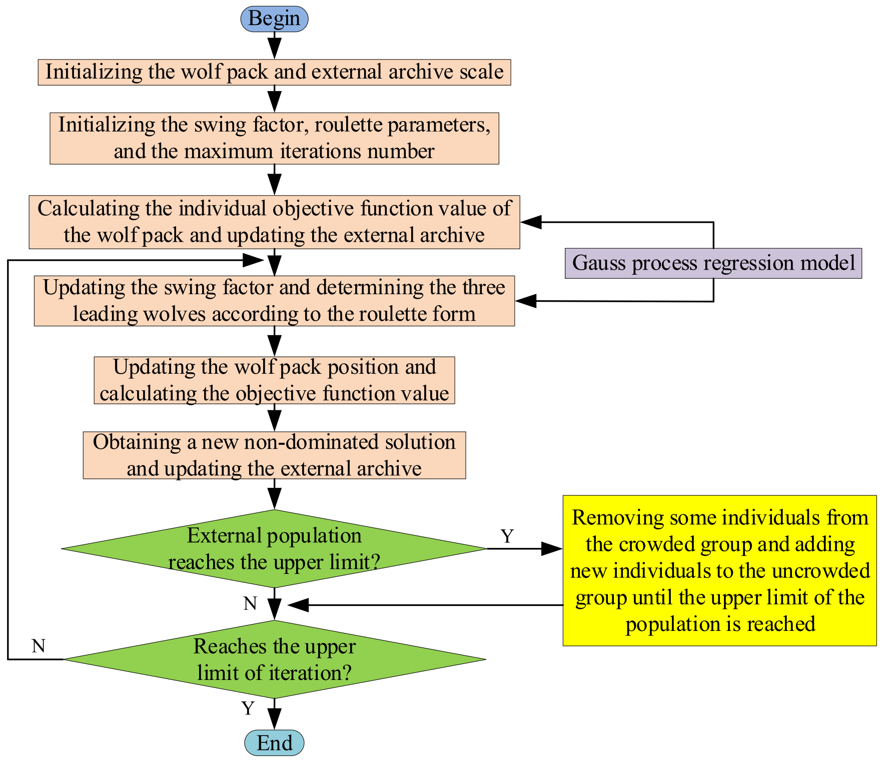

Figure 13. Flow chart of multi-objective gray wolf optimization algorithm.

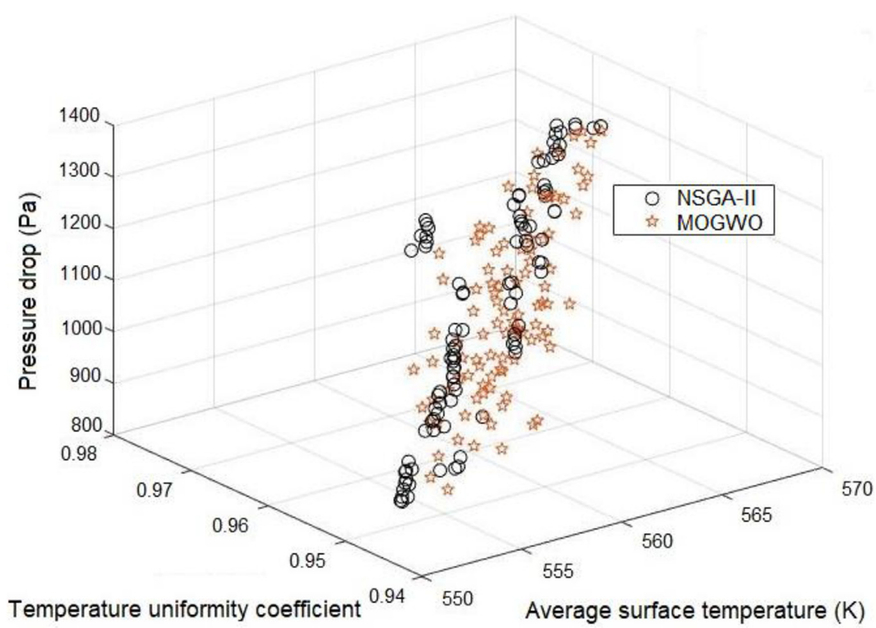

Figure 14. Optimal solution set based on MOGWO and NSGA-II.

Table 6. Comparison results of compatibility performance index.

Algorithm	η_{max}	η_{min}	η_{ave}
NSGA-II	0.918	0.874	0.894
MOGWO	0.923	0.877	0.896

of TEG system, and its flow chart is shown in Figure 13. On this occasion, the grey wolf population, the maximum iteration number and the external population archive are all set to be 100.

To validate the advantage of MOGWO, it is compared with the classical Non-Dominated Sorted Genetic Algorithm-II (NSGA-II) [36], whose initial population size is 100, maximum iterations number is 100, genetic crossover probability is 0.9, and mutation probability is 0.25. The non-inferior solution results obtained with both MOGWO and MOGWO are shown in Figure 14. It can be observed that the distribution of Pareto solution set based on MOGWO and the one based on NSGA-II coincide on the whole. The former is dispersed and uniform with better diversity, while the latter is relatively concentrated.

Table 7. Several other fin parameters for comparison.

Case	L	W	A	S
Case 1	35 mm	7 mm	75°	20 mm
Case 2	37 mm	8 mm	80°	30 mm
Case 3	39 mm	9 mm	85°	25 mm

The constraint condition of non-inferior solution is set as: $T_f \geq 555$ K, $\lambda_f \geq 0.95$ and $\Delta P_f \leq 1000$ Pa. In addition, to well balance T_{ave}, γ and P_d, the constrained optimization solution set based on MOGWO and NSGA-II is transformed respectively with the compatibility performance indexes (denoted η), which can be calculated using Eq. (29).

$$\eta = \frac{\frac{T_j}{T_0} \times \frac{\lambda_j}{\lambda_0}}{\frac{\Delta P_j}{\Delta P_0}} \tag{29}$$

where T_{j}, λ_{j} and ΔP_{j} are the T_{ave}, γ and P_d of the jth PS heat exchanger shown in Figure 2, T_0, λ_0 and ΔP_0 are the corresponding ones of the jth empty cavity structure based PS heat exchanger.

Table 6 lists the compared compatibility performance indexes based on MOGWO and NSGA-II. The maximum, minimum and average compatibility performance index (denoted η_{max}, η_{min} and η_{ave}, respectively) of MOGWO optimization solution set is larger than that with NSGA-II, which indicates that MOGWO is feasible to optimize the PS heat exchanger.

In all, the optimized fin parameters corresponding to the maximum compatibility performance index of Pareto solution set based on MOGWO is: $L = 34.86$ mm, $W = 7.66$ mm, $A = 71.48°$, $S = 20.70$ mm. In this case, the corresponding average surface temperature is 555.68 K, temperature uniformity is 0.95 and pressure drop is 935.79 Pa. Besides, the corresponding simulated results with the same optimized fin parameters is 555.06 K, 0.952 and 939.07 Pa, respectively. Compared with the optimization results, the differences are 0.11%, 0.21% and 0.35%, respectively (i.e. less than 1%), which further validates the feasibility of the established gauss process regression agent model.

Table 8. Comparison results of compatibility performance index.

	Cavity	Optimized	Case 1	Case 2	Case 3
η	-	0.923	0.905	0.778	0.722

5. Results and discussion

5.1. Compatibility performance index

To validate the compatibility performance of the above optimized heat exchanger, several other fin parameters different from the above 16 orthogonal experimental samples are listed in Table 7.

When the exhaust flow rate and temperature is set to be 40 m/s and 600 K, respectively, Figure 15 compares the performance of the empty cavity structure based heat exchanger with other ones. It can be seen that T_{ave} of the optimized PS heat exchanger increases from 545.1 K to 555.1 K (increased by 1.83%, see Figure 15a), the maximum surface temperature (denoted T_{max}) increases from 552.5 K to 561.3 K (increased by 1.59%, see Figure 15b) the pressure loss increases from 853.8 Pa to 939.1 Pa (increased by 9.99%, see Figure 15d), while the temperature uniformity decreased from 0.957 to 0.952 (decreased by 0.52%, see Figure 15c). Despite of the increased pressure drop, the effect of the optimized PS heat exchanger on the ICE performance is limited, and the temperature uniformity variation is within the acceptable range.

In addition, compared with the heat exchangers in case 1 and case 2, T_{ave} of the optimized PS heat exchanger is reduced by 0.01% and 0.93%, T_{max} is reduced by 0.04% and 0.82%, the pressure drop is reduced by 1.46% and 15.29%, while the temperature uniformity is increased by 0.21% and 1.28%, respectively. Although the optimized PS heat exchanger displays decreased T_{ave} and T_{max}, its pressure drop is much

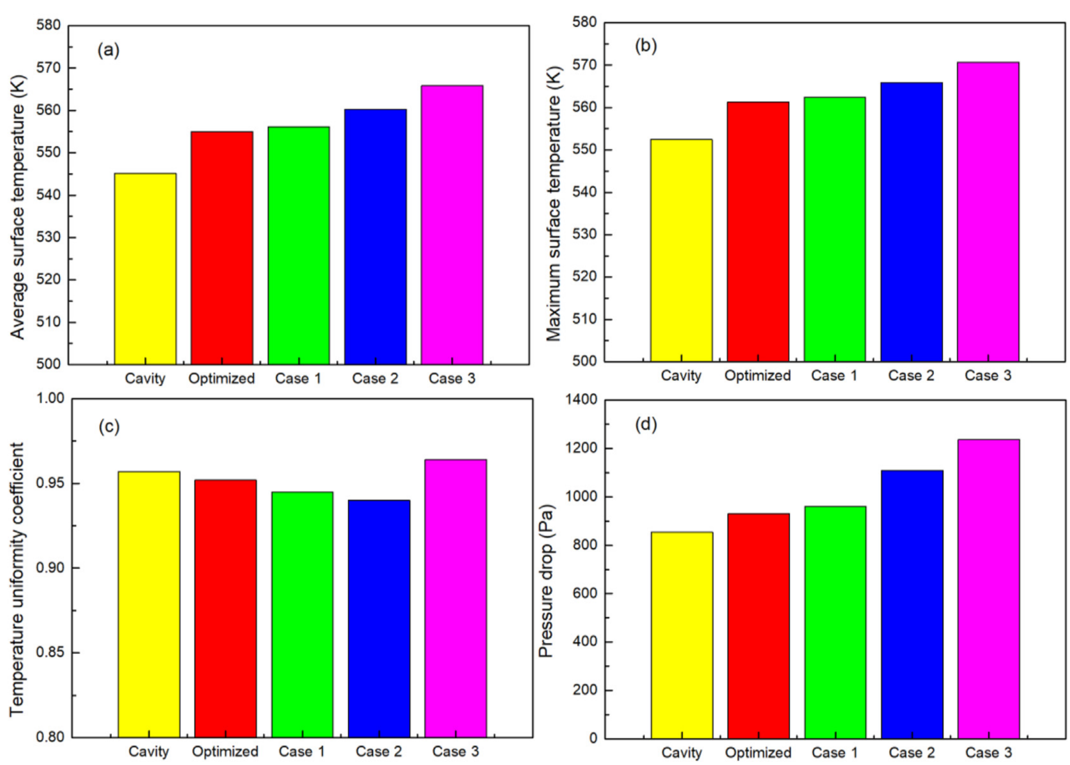

Figure 15. Performance comparison of different heat exchangers. (a) T_{ave}; (b) T_{max}; (c) γ; (d) P_d.

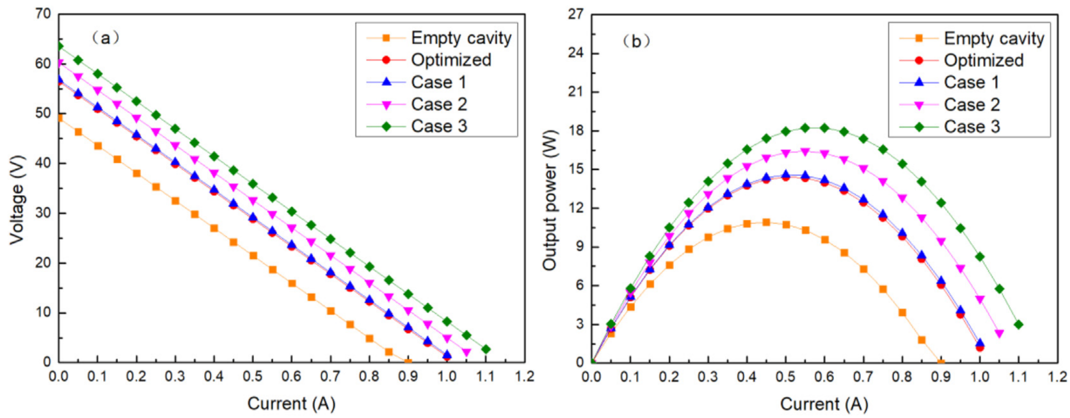

Figure 16. The voltage-current and power-current curves of TEG system. (a) voltage-current curve; (b) power-current curve.

smaller, and it has more uniform temperature distribution when it is applied in automobile exhaust recovery.

Finally, the T_{ave}, T_{max}, P_d and γ of the optimized PS heat exchanger are decreased by 1.91%, 1.68%, 24.06% and 1.24% respectively compared with the one in case 3. In all, the optimized one has significant pressure drop reduction and much smaller impact on ICE exhaust.

Table 8 lists the compatibility performance index comparison results before and after optimization. The optimized one has a higher compatibility performance index than those in case 1, case 2 and case 3, and displays similar performance to the one in case 1. Although the optimized heat exchanger has lower transfer performance than the ones in case 2 and case 3, its smaller pressure drop makes it insignificant.

5.2. Output power and thermoelectric conversion efficiency

Based on the above Pareto solution set, the optimized fin parameters are as follows: $L = 34.86$ mm, $W = 7.66$ mm, $A = 71.48°$, $S = 20.7$ mm. Then, the output performance of TEG using different heat exchangers is compared on the same boundary conditions listed in Table 1.

The voltage-current and power-current curves of TEG system are shown in Figure 16 at the maximum flow rate when the inlet exhaust temperature is set to be 600 K. Obviously, compared with the TEG system using empty cavity structure based PS heat exchanger, the optimized TEG system outputs greater voltage (see Figure 16a) and higher power (see Figure 16b) with the same output current. The optimized TEG system has similar output performance to the one in case 1, but has smaller output performance than that in both case 2 and case 3. Thus, the heat exchangers in case 2 and case 3 have higher surface temperature, which increases the temperature difference of TEMs and enhance the open-circuit voltage of TEG on the same occasion.

Furthermore, the maximum output power of TEG systems is compared in Figure 17. Compared with the TEG system using the empty cavity structure based PS heat exchanger, P_{max} of the optimized one is increased from 10.92 W to 14.43 W, which is increased by 32.1%. Besides, the optimized TEG system has similar P_{max} to the one in case 1. Compared with TEG system in case 2 (16.45 W) and case 3 (18.26 W), P_{max} of the optimized one is decreased by 12.27% and 20.97%, respectively.

The heat flows into TEG system (denoted Q_f) is calculated using Eq. (30) [37].

$$Q_f = C_f \rho_f G_f \Delta T_f = C_f \rho_f G_f (T_{in} - T_{out}) \tag{30}$$

where C_f is the heat capacity, ρ_f means the density, G_f represnts the volume flow, T_{in} and T_{out} corresponding to the inlet and outlet exhaust temperature. In this cas, the calculated maximum thermoelectric conversion efficiency (denoted η_{TEG}) is defined by Eq. (31).

$$\eta_{TEG} = P_{max} / Q_f \tag{31}$$

Figure 18 shows the maximum thermoelectric conversion efficiency of TEG, which indicates that it has the same variation trend as P_{max} shown in Figure 17. Compared with the TEG system using heat exchanger without fins, the maximum output power of the optimized one is increased from 0.34 % to 0.43%, which is increased by 30.3% and is equivalent to the one in case 1 (i.e. 0.44%). Compared with η_{TEG} of TEG

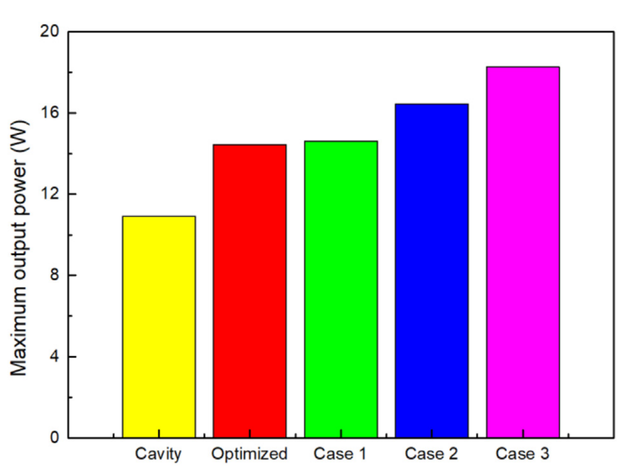

Figure 17. Output power comparison of different TEG systems.

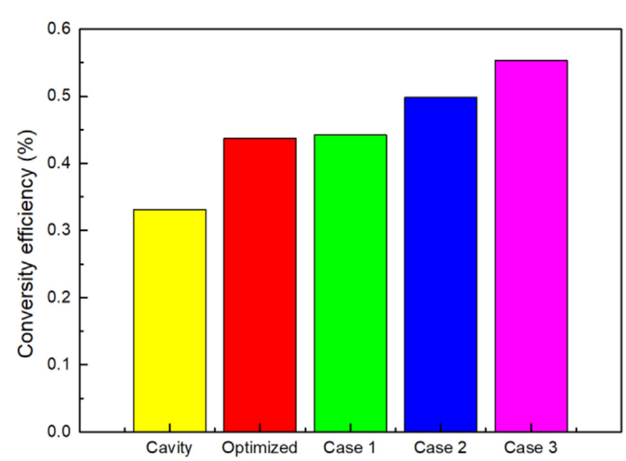

Figure 18. Maximum thermoelectric conversion efficiency comparison of different TEG systems.

systems in case 2 and case 3 (0.49% and 0.55 %), the one of the optimized TEG is decreased by 10.2% and 21.8%, respectively.

Considering the pressure drop of optimized PS heat exchanger is smaller than those in case 2 and case 3, it can be conclude that the optimized PS heat exchanger not only ensures satisfactory power generation and thermoelectric conversion efficiency, but also meets the compatibility requirements by reducing exhaust pressure drop and maintaining a relatively high temperature uniformity when it is applied in exhaust heat recovery.

6. Conclusions

To evaluate the heat transfer, fluid flow and fluid-solid-heat coupling effects, the performance of a PS heat exchanger for automobile exhaust recovery was analyzed using the realizable k-ϵ turbulence model from the aspect of different fin parameters. Both simulation and experimental results demonstrate that increasing L, W and A improves the heat transfer and power generation of TEG system. Nevertheless, the temperature uniformity is not obviously affected by increasing S, which decrease its maximum power and deteriorates its temperature uniformity.

In addition, according to the ANOVA method, the influence order for the T_{ave} is $L > W > S > A$, the one for γ is $L > S > A > W$, and the one for P_d is $L > W > A > S$. To ensure low backpressure, large output power and good temperature uniformity, the designed compatibility optimization objective function is optimized with MOGWO, and the non-inferior solution of final Pareto solution set is selected according to the highest compatibility performance index.

Compared with the TEGs using the empty cavity based PS heat exchanger and other kinds of PS heat exchangers, the optimized TEG system well balances pressure drop, temperature uniformity, thermoelectric conversion efficiency and power generation, and it can reduce the impact on ICE performance when it is applied in automobile exhaust recovery.

To establish the realizable k-ϵ turbulence model of TEG system, several assumptions were put forward to simplify the calculation, and the dynamic response characteristics of TEG under transient temperature excitations remains to be considered. Even though TEG can generate electric power when the heat exchanger is added to harvest exhaust heat, the effect of TEG on the original performance of ICE and their performance interaction is our ongoing research work, which can provide a theoretical reference to the compatibility optimization, energy saving and emission reduction evaluation of low-backpressure AETEGs in further.

Declarations

Author contribution statement

Rui Quan: Conceived and designed the experiments; Wrote the paper.

Junhui Wang: Performed the experiments; Analyzed and interpreted the data.

Tao Li: Contributed reagents, materials, analysis tools or data.

Funding statement

Professor Rui Quan was supported by National Natural Science Foundation of China [51977061, 51407063], the Open Foundation of Hubei Key Laboratory for High-efficiency Utilization of Solar Energy and Operation Control of Energy Storage System [HBSEES202205].

Data availability statement

Data will be made available on request.

Declaration of interest's statement

The authors declare no conflict of interest.

Additional information

No additional information is available for this paper.

References

[1] Z.G. Shen, L.L. Tian, X. Liu, Automotive exhaust thermoelectric generators: current status, challenges and future prospects, Energy Convers. Manag. 195 (2019) 1138–1173.
[2] R. Ramírez-Restrepo, A. Sagastume-Gutiérrez, J. Cabello-Eras, B. Hernández, J. Duarte-Forero, Experimental study of the potential for thermal energy recovery with thermoelectric devices in low displacement diesel engines, Heliyon 7 (2021), e08273.
[3] A. Riahi, A. Ben, A. Fadhel, A. Guizani, M. Balghouthi, Performance investigation of a concentrating photovoltaic thermal hybrid solar system combined with thermoelectric generators, Energy Convers. Manag. 205 (2020), 112377.
[4] T.C. Holgate, R. Bennett, T. Hammel, T. Caillat, S. Keyser, B. Sievers, Increasing the efficiency of the multi-mission radioisotope thermoelectric generator, J. Electron. Mater. 44 (2015) 1814–1821.
[5] B. Iezzi, K. Ankireddy, J. Twiddy, M. Losego, J. Jur, Printed, metallic thermoelectric generators integrated with pipe insulation for powering wireless sensors, Appl. Energy 208 (2017) 758–765.
[6] R. Quan, G.Y. Liu, C.J. Wang, W. Zhou, L. Huang, Y.D. Deng, Performance investigation of an exhaust thermoelectric generator for military SUV application, Coatings 8 (2018) 45.
[7] Y. Ge, Z. Liu, H. Sun, W. Liu, Optimal design of a segmented thermoelectric generator based on three-dimensional numerical simulation and multi-objective genetic algorithm, Energy 147 (2018) 1060–1069.
[8] A.B. Amar, A. Kouki, H. Cao, Power approaches for implantable medical devices, Sensors 15 (2015) 28889–28914.
[9] M. Thielen, L. Sigrist, M. Magno, C. Hierold, L. Benini, Human body heat for powering wearable devices: from thermal energy to application, Energy Convers. Manag. 131 (2017) 44–54.
[10] B. Orr, A. Akbarzadeh, M. Mochizuki, R. Singh, A review of car waste heat recovery systems utilising thermoelectric generators and heat pipes, Appl. Therm. Eng. 101 (2016) 490.
[11] Y. Zhang, M. Cleary, X. Wang, N. Kempf, L. Schoensee, J. Yang, G. Joshi, L. Meda, High-temperature and high-power-density nanostructured thermoelectric generator for automotive waste heat recovery, Energy Convers. Manag. 105 (2015) 946–950.
[12] F.P. Brito, J. Martins, E. Hançer, N. Antunes, L.M. Gonçalves, Thermoelec heat recovery with heat pipe-based thermal control, J. Electron. Mater. 44 (2015) 1984–1997.
[13] S.K. Kim, B.C. Won, S.H. Rhi, S.H. Kim, J.H. Yoo, J.C. Jang, Thermoelectric power generation system for future hybrid vehicles using hot exhaust gas, J. Electron. Mater. 40 (2011) 778–783.
[14] N. Muralidhar, M. Himabindu, R.V. Ravikrishna, Modeling of a hybrid electric heavy duty vehicle to assess energy recovery using a thermoelectric generator, Energy 148 (2018) 1046–1059.
[15] S. Kumar, S.D. Heister, X. Xu, J.R. Salvador, G.P. Meisner, Thermoelectric generators for automotive waste heat recovery systems Part II: parametric evaluation and topological studies, J. Electron. Mater. 42 (2013) 944–955.
[16] T.Y. Kim, J. Kwak, B.W. Kim, Energy harvesting performance of hexagonal shaped thermoelectric generator for passenger vehicle applications: an experimental approach, Energy Convers. Manag. 160 (2018) 14–21.
[17] R. Quan, C.J. Wang, F. Wu, Y.F. Chang, Y.D. Deng, Parameter matching and optimization of an isg mild hybrid powertrain based on an automobile exhaust thermoelectric generator, J. Electron. Mater. 49 (2020) 2734–2746.
[18] C.C. Weng, M.J. Huang, A simulation study of automotive waste heat recovery using a thermoelectric power generator, Int. J. Therm. Sci. 71 (2013) 302–309.
[19] H.Q. Yang, G.Q. Shu, Hua Tian, Xn Ma, Ty Chen, Peng Liu, Optimization of thermoelectric generator (TEG) integrated with three-way catalytic converter (TWC) for harvesting engine's exhaust waste heat, Appl. Therm. Eng. 14 (2018) 628–638.
[20] Y.D. Deng, X. Liu, S. Chen, N.Q. Tong, Thermal Optimization of the heat exchanger in an automotive exhaust-based thermoelectric generator, J. Electron. Mater. 42 (2013) 1634–1640.
[21] J.H. Yang, F.R. Stabler, Automotive applications of thermoelectric materials, J. Electron. Mater. 38 (2009) 1245–1251.
[22] C.N. Michos, S. Lion, I. Vlaskos, R. Taccani, Analysis of the backpressure effect of an Organic Rankine Cycle (ORC) evaporator on the exhaust line of a turbocharged heavy duty diesel power generator for marine applications, Energy Convers. Manag. 132 (2017) 347–360.
[23] S. Li, Y.P. Wang, T. Wang, X. Yang, Y.D. Deng, C.Q. Su, Optimization of heat exchangers with dimpled surfaces to improve the performance in thermoelectric generators using a Kriging model, J. Electron. Mater. 46 (2017) 3062–3070.
[24] R. Quan, W.L. Liang, S.L. Quan, Z.K. Huang, Z.Z. Liu, Y.F. Chang, B.H. Tan, Performance interaction assessment of automobile exhaust thermoelectric generator and engine under different operating conditions, Appl. Therm. Eng. 216 (2022), 119055.
[25] W. Zhou, J. Yang, Q. Qin, J. Zhu, S. Xu, D. Luo, R. Wang, Research on module layout and module coverage of an automobile exhaust thermoelectric power generation system, Energies 15 (2022) 987.
[26] R. Quan, X.F. Tang, S.H. Quan, L. Huang, A novel optimization method for the electric topology of thermoelectric modules used in an automobile exhaust thermoelectric generator, J. Electron. Mater. 42 (2013) 1469–1475.

[27] C.Y. Zhu, Y.T. Zhang, T. Wu, Z.H. He, T. Guo, N.P. Feng, Optimizing glycerosome formulations via an orthogonal experimental design to enhance transdermal triptolide delivery, Acta Pharm. 72 (2022) 135–146.
[28] M.C. Cao, H.Y. Zhao, R.Q. Xie, L.Y. Zhao, S.J. Zhao, J.F. Bai, Multiparameter optimization design of chemical mechanical polishing for planar optics, Int. J. Adv. Manuf. Technol. 12 (2021) 1–10.
[29] S.L. Siedlecki, J.F. Bena, What the clinical nurse specialist should know about analysis of variance tests, Clin. Nurse Spec. 36 (2022) 10–15.
[30] M. Marsman, L. Waldorp, F. Dablander, E.J. Wagenmakers, Bayesian estimation of explained variance in ANOVA designs, Stat. Neerl. 73 (2019) 351–372.
[31] Y.Q. Yan, Variance analysis of software ageing problems, IET Softw. 12 (2018) 41–48.
[32] Z. Ma, W.X. Pan, Data-driven nonintrusive reduced order modeling for dynamical systems with moving boundaries using Gaussian process regression, Comput. Methods Appl. Math. 373 (2021), 113495.
[33] M. Leco, V. Kadirkamanathan, A perturbation signal based data-driven Gaussian process regression model for in-process part quality prediction in robotic countersinking operations, Robot. Cim-Int. Manuf. 71 (2021), 102105.
[34] S. Mirjalili, S.M. Mirjalili, A. Lewis, Grey wolf optimizer, Adv. Eng. Software 69 (2014) 46–61.
[35] S. Mirjalili, S. Saremi, S.M. Mirjalili, S.M. Mirjalili, L.S. Coelho, Multi-objective grey wolf optimizer: a novel algorithm for multi-criterion optimization, Expert Syst. Appl. 47 (2015) 106–119.
[36] S. Fettaka, J. Thibault, Y. Gupta, A new algorithm using front prediction and NSGA-II for solving two and three-objective optimization problems, Optim. Eng. 16 (2015) 713–736.
[37] X. Niu, J.L. Yu, S.Z. Wang, Experimental study on low-temperature waste heat thermoelectric generator, J. Power Sources 188 (2009) 621–626.